

# The MAVEN Solar Energetic Particle Investigation

Davin E. Larson<sup>1</sup> · Robert J. Lillis<sup>1</sup> · Christina O. Lee<sup>1</sup> · Patrick A. Dunn<sup>1</sup> · Kenneth Hatch<sup>1</sup> · Miles Robinson<sup>1</sup> · David Glaser<sup>1</sup> · Jianxin Chen<sup>2</sup> · David Curtis<sup>1</sup> · Christopher Tiu<sup>1</sup> · Robert P. Lin<sup>1</sup> · Janet G. Luhmann<sup>1</sup> · Bruce M. Jakosky<sup>3</sup>

Received: 29 March 2015 / Accepted: 19 October 2015 / Published online: 5 November 2015  
© Springer Science+Business Media Dordrecht 2015

**Abstract** The MAVEN Solar Energetic Particle (SEP) instrument is designed to measure the energetic charged particle input to the Martian atmosphere. SEP consists of two sensors mounted on corners of the spacecraft deck, each utilizing a dual, double-ended solid-state detector telescope architecture to separately measure fluxes of electrons from 20 to 1000 keV and ions from 20–6000 keV, in four orthogonal look directions, each with a field of view of 42° by 31°. SEP, along with the rest of the MAVEN instrument suite, allows the effects of high energy solar particle events on Mars’ upper atmospheric structure, temperatures, dynamics and atmospheric escape rates, to be quantified and understood. Given that solar activity was likely substantially higher in the early solar system, understanding the relationship between energetic particle input and atmospheric loss today will enable more confident estimates of total atmospheric loss over Mars’ history.

## 1 Introduction to the SEP Instrument

### 1.1 Scientific Objectives

The Mars Atmosphere and Volatile EvolutionN (MAVEN) mission (Jakosky et al. 2014) has three major science objectives: (1) determine the current state of the upper atmosphere and the processes that control it, (2) measure the escape rate of atmospheric gases to space during the present epoch and determine how the escape rate depends on the controlling processes, and (3) extrapolate to the total atmospheric loss to space over Mars’ history. Solar energetic particles (SEPs) are an important, if irregular, source of energy input into the Martian atmosphere. We know from terrestrial observations that precipitating SEPs cause

---

✉ R.J. Lillis  
[rlillis@ssl.berkeley.edu](mailto:rlillis@ssl.berkeley.edu)

<sup>1</sup> Space Science Laboratory, University of California, 7 Gauss Way, Berkeley, CA 94720, USA

<sup>2</sup> Baja Technology LLC, 1040 East 4th St Gould-Simpson 235, Tucson, AZ 85721, USA

<sup>3</sup> Laboratory for Atmospheric and Space, University of Colorado, 1234 Innovation Drive, Boulder, CO 80303, USA

direct heating, ionization, dissociation, excitation and charge exchange (e.g. Reagan and Watt 1976). At Earth, these effects also lead to secondary photochemical changes in the atmosphere (e.g. Chevalier et al. 2007; Dmitriev and Yeh 2008). Compared with the terrestrial case, measurements of SEP effects at Mars are relatively scarce. SEPs were first measured at Mars by the SLED instrument on Phobos-2 (McKenna-Lawlor et al. 1992) and later by the Martian Radiation Environment Experiment (MARIE) on board the Mars Odyssey spacecraft (Zeitlin et al. 2004). Evidence of SEP-produced ionization in the upper thermosphere were observed by the Mars Global Surveyor Magnetometer/Electron Reflector (MAG/ER) instrument (Mitchell et al. 2001) from the detection of SEP-produced secondary electrons (Lillis et al. 2012). Observations from Mars Advanced Radar for Sub-surface and Ionosphere Sounding (MARSIS) on Mars Express showed evidence of SEP-produced ionization below the main ionospheric peak from the disappearance of radar reflections from the Martian surface (Morgan et al. 2006; Espley et al. 2007). From ASPERA-3 on board Mars Express (Barabash et al. 2006), a correlation was shown between the detection of the SEPs and an order-of-magnitude increase in the heavy atmospheric ion escape during major solar flare event (Futaana et al. 2008). There have also been observations of aurorae related to SEPs from the Mars Express Spectroscopy for Investigation of Characteristics of the Atmosphere of Mars (SPICAM) instrument (Bertaux et al. 2005; Leblanc et al. 2006). At the Martian surface, secondary neutrons produced by SEPs in the upper atmosphere were detected (Hassler et al. 2014) by the Radiation Assessment Detector (RAD) (Hassler et al. 2012) on board the Mars Science Laboratory (MSL).

At Mars, SEP ions with energies below a few hundred keV/nuc deposit their energies above the homopause ( $\sim 120$  km altitude), i.e. in the primary reservoir for atmospheric escape. Thus, this energy range is the most important for the MAVEN SEP experiment. While SEPs in this energy range have been measured in the Mars near-space environment by the Phobos SLED, these measurements have never been made in concert with the unprecedented set of magnetic field, plasma and neutral measurements by the other MAVEN instruments. These measurements can put the SEP measurements in the broader context of space weather at Mars, its effects on the atmosphere, and the atmospheric escape rates (Lillis et al. 2015).

The magnetometer (MAG) (Connerney et al. 2015), Solar Wind Ion Analyzer (SWIA) (Halekas et al. 2013) and Solar Wind Electron Analyzer (SWEA) provide heliophysical context for the SEP measurements when MAVEN is in the solar wind, i.e. the configuration of the interplanetary magnetic field and the speed and density of solar plasma. The EUV experiment (Eparvier et al. 2015) provides the relative timing of solar flares with respect to SEP particles, giving clues as to whether their origins lie at the Sun and/or interplanetary shock. The Suprathermal and Thermal Ion Composition (STATIC) experiment (McFadden et al. 2015) can detect ion heating due to SEP precipitation as well as increases in pickup ion escape during SEP events, as have been measured by the Mars Express IMA instrument (Futaana et al. 2008). The Langmuir Probe & Waves (LPW) (Andersson et al. 2015) experiment measures increases of the electron density in the Mars ionosphere due to SEP ionization, while the Neutral Gas and Ion Mass Spectrometer (NGIMS) (Mahaffy et al. 2014) can record neutral temperature increases, as well as increased ion concentration and photochemical consequences of SEP precipitation, all in situ. Lastly, the Imaging Ultraviolet Spectrometer (IUVS) (McClintock et al. 2014) can detect thermospheric SEP consequences remotely.

## 1.2 Driving Requirements

The scientific goals of the MAVEN mission and spacecraft accommodation each drive the design of the SEP instrument. The requirements were set to allow a basic determination

**Table 1** Comparison of the SEP Level 1 requirements versus the instrument performance

Requirement (ions only)	MAVEN Level 1 requirement	SEP instrument performance
Energy range	50 keV to 5 MeV	20 keV to 6 MeV
Energy resolution $\Delta E/E$	50 %	< 25 % (better at lowest energy)
Energy flux range	10 to $10^6$ eV/[cm <sup>2</sup> s sr eV]	3 to $3 \times 10^6$ eV/[cm <sup>2</sup> s sr eV]
Energy flux precision	30 %	< 10 % (based on modelling)
Time cadence	1 hour	1–32 seconds (mode-dependent)

of the solar energetic particle input into the Martian atmosphere. First, this required a field of view (FOV) coverage sufficiently wide to characterize particles striking Mars, regardless of the spacecraft orientation, which is ensured by four  $42^\circ \times 31^\circ$  orthogonal fixed FOV. Second, SEP requires sufficient cadence, dynamic range and energy range and resolution to adequately characterize the huge variability in the SEP environment at Mars. Overall, the SEP instrument satisfies and, in most cases, significantly exceeds the Level 1 MAVEN requirement to determine solar energetic particle characteristics, as shown in Table 1. Note that, although the SEP instrument measures electrons, there was no requirement to do so.

### 1.3 Heritage

The SEP sensors, described in Sect. 2, are closely based on the Solid State Telescope (SST) sensors on the THEMIS probes (Angelopoulos et al. 2008) and also share significant heritage with the SupraThermal Electron (STE) detectors on STEREO (Lin et al. 2008), the SEPT detectors on STEREO (Müller-Mellin et al. 2008) and the SST detectors on the Wind spacecraft (Lin et al. 1995). Major differences from THEMIS SST affecting science are (1) a wider field of view for each aperture ( $42^\circ \times 31^\circ$  vs.  $42^\circ \times 23^\circ$ ) to better characterize SEP flux, (2) a thinner Kapton foil (2.43  $\mu\text{m}$  vs. 4.3  $\mu\text{m}$ ) to allow detection of electrons down to  $\sim 20$  keV (versus  $\sim 30$  keV) and (3) a substantially thicker layer (900  $\text{\AA}$  vs. 200  $\text{\AA}$ ) of vapor-deposited aluminum (VDA) on the bare detectors to reduce photo induced leakage current and subsequent noise from Mars-shine.

## 2 SEP Instrument Description

The SEP instrument consists of 2 sensors, SEP1 and SEP2, each consisting of a pair of double-ended solid-state telescopes, measuring electrons and ions over the energy ranges  $\sim 20$ –1000 keV and  $\sim 20$ –6000 keV respectively. Figures 1 and 2 show the SEP sensors and the labeling of the apertures.

### 2.1 Mounting and Fields of View

The SEP sensors are mounted on two corners of the top deck of the spacecraft as shown in Fig. 3 (top panel). This deck, to which the +Z-direction is normal in spacecraft coordinates, faces the Sun during most of each orbit with the exception of the periapsis segment (Jakosky et al. 2014). The SEP FOVs, as illustrated in Fig. 3 (bottom panel), are positioned to adequately cover the canonical Parker spiral direction around which solar energetic particle distributions are centered, at least in a statistical sense, while always avoiding glint

**Fig. 1** The two identical SEP sensors. The *red covers* are placed over the collimators to protect the detectors from contamination and were removed before flight

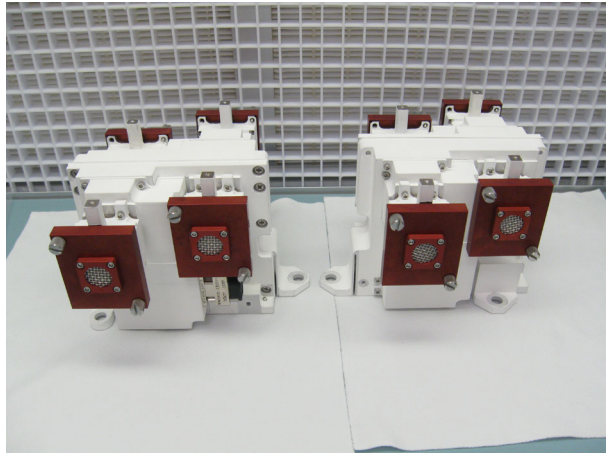
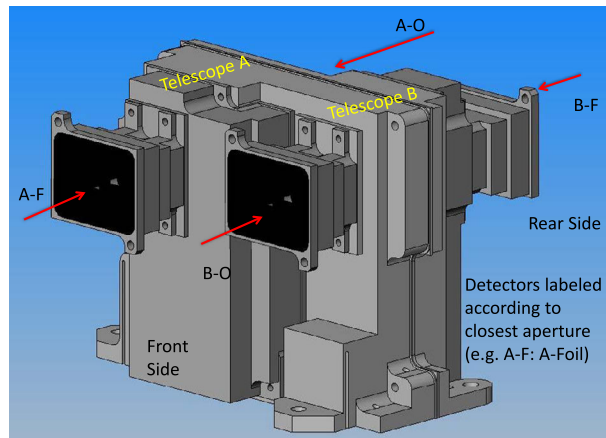


**Fig. 2** Perspective view of the SEP sensor identifying particle directions (*red arrows*). Each aperture is labeled with the name of the detector facing that aperture. Also shown are the sensor coordinate system, the telescope identifier A or B, and the front and rear sides of the sensor. The collimators are the *large black areas* and define the FOV



from the spacecraft, the other sensors, and the Articulated Payload Platform (APP), and also avoiding direct sunlight during spacecraft attitudes typical of normal science operations.

## 2.2 Instrument Configuration and Detectors

A strong magnetic field, provided by strong permanent magnets, is required to allow separation of electrons from ions. However, stray magnetic fields must be minimized because MAVEN carries a magnetometer (Connerney et al. 2015). This requires the SEP design to have a closed magnetic field configuration with oppositely directed magnetic fields for each telescope, which in turn requires a yoke. Therefore the most economical design is a dual double-ended telescope arranged in an offset configuration around the yoked magnet, as shown in Fig. 4 (top). The telescopes are referred to by their “Telescope ID” (TID) as ‘A’ and ‘B’. At opposite ends of each telescope are baffled collimators with identical apertures measuring  $42^\circ \times 31^\circ$ .

Each telescope consists of a stacked triplet of doped silicon detectors, as shown in Fig. 4 (bottom). The outer detectors of the stack are  $300\ \mu\text{m}$  thick, while the middle detector consists of two  $300\ \mu\text{m}$  detectors wire-bonded together, making an effective thickness of

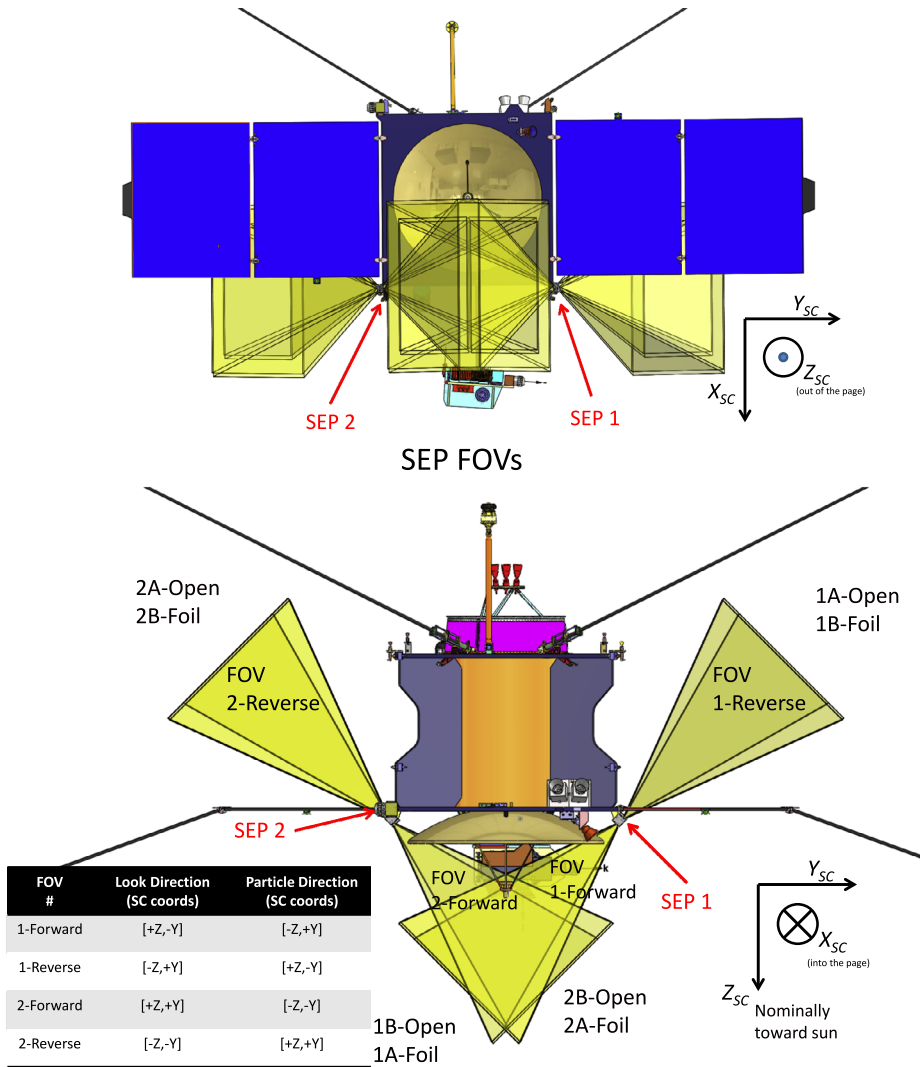


**Fig. 3** The location (*top panel*) and FOVs (*bottom panel*) of the SEP sensors on the spacecraft with the spacecraft coordinate system shown. The spacecraft Z-direction nominally points toward the Sun except near periapsis

600  $\mu\text{m}$ . One side of the detector stack is covered with a 2.43  $\mu\text{m}$  Al-Kapton-Al foil to stop ions with energies of  $< 250$  keV/nuc, and is known as the “Foil” side. The 300  $\mu\text{m}$  detector on the “Foil” side of the stack (i.e. closest to the foil) is referred to as the “F” detector. On the opposite side of the detector stack is the aforementioned strong magnetic field ( $\sim 0.25$  T, created by yoked Sm-Co magnets), to sweep away all electrons with energies  $< 350$  keV, and is known as the “Open” side. The 300  $\mu\text{m}$  detector on the “Open” side is known as the “O” detector and is coated with  $\sim 900$   $\text{\AA}$  of aluminum to prevent reflected light from sunlit Mars from increasing the leakage current and the corresponding detector noise. The 600  $\mu\text{m}$  middle detector is known as the “Thick” or “T” detector. The apertures closest to

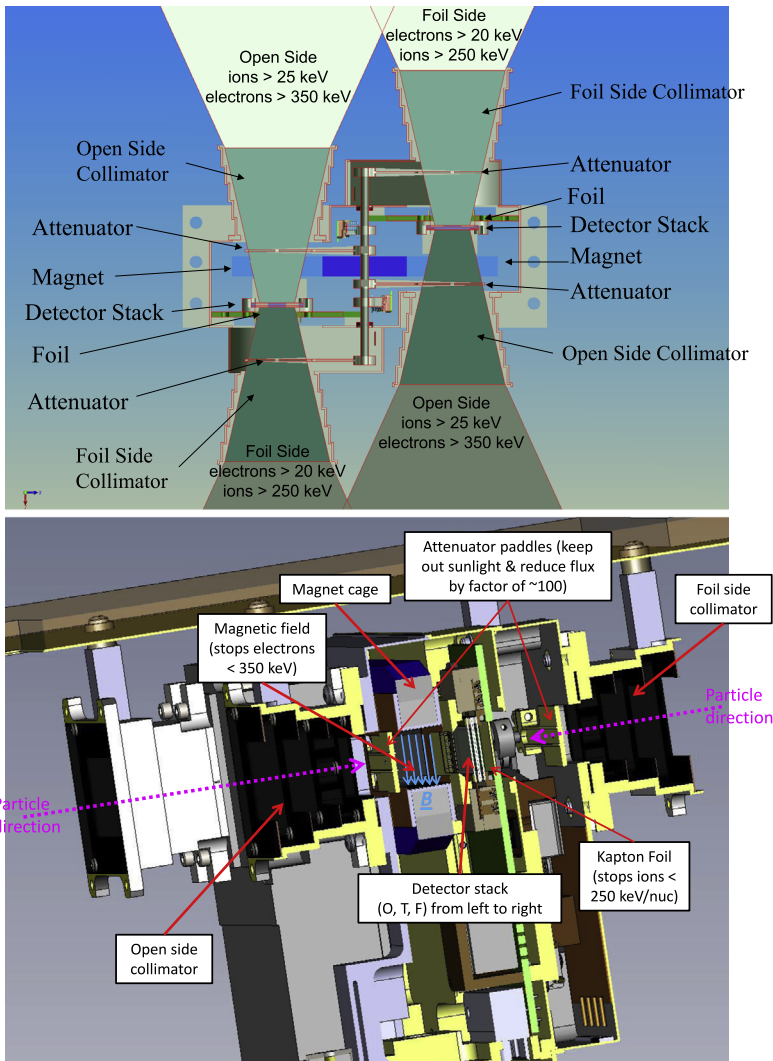


**Fig. 4** Illustrations of the SEP sensor optics layout. The *top panel* shows a top-down view of one SEP sensor unit. Note that both telescopes share a single magnet cage with oppositely-directed fields for each telescope, to minimize external magnetic fields. The *bottom panel* shows a side view of one SEP sensor with a cross section to highlight the features of each telescope

the “Foil” and “Open” sides of the detector stack are called the “Foil” and “Open” apertures respectively, as shown in Fig. 4 (top panel). Table 2 shows the mapping between SEP sensor, detector stack (TID), aperture, detector and FOV.

Each sensor unit has 4 co-moving attenuator paddles with small pinholes which can be rotated into the FOVs of both sides of both detector stacks to reduce particle fluxes by a factor of  $\sim 100$  and to prevent direct sunlight from overheating and damaging the detectors. With the attenuators open, the FOV has a roughly triangular response function and is much flatter (but nearly same width) than with the attenuators closed. The interior structure of the SEP instrument is shown in Fig. 4 (bottom panel).

**Table 2** Relationship between the SEP sensor number and field of view label shown in Fig. 3 to the detector stack letter, aperture name and closest detector shown in Figs. 2 and 4

SEP sensor	Detector stack (TID)	Aperture	Closest detector	Primary particle detected	FOV #	Look direction (SC coords)	Particle direction (SC coords)
1	A	Foil	1AF	Electrons	1-Forward	[+Z, -Y]	[-Z, +Y]
		Open	1AO	Ions	1-Reverse	[-Z, +Y]	[+Z, -Y]
1	B	Foil	1BF	Electrons	1-Reverse	[-Z, +Y]	[+Z, -Y]
		Open	1BO	Ions	1-Forward	[+Z, -Y]	[-Z, +Y]
2	A	Foil	2AF	Electrons	2-Forward	[+Z, +Y]	[-Z, -Y]
		Open	2AO	Ions	2-Reverse	[-Z, -Y]	[+Z, +Y]
2	B	Foil	2BF	Electrons	2-Reverse	[-Z, -Y]	[+Z, +Y]
		Open	2BO	Ions	2-Forward	[+Z, +Y]	[-Z, -Y]

### 2.3 Detector Signal Processing

SEP does not calculate electron or ion count rates on board because electrons and ions can mimic each other in terms of the amount of energy deposited and the detector in which it is deposited. Instead, each sensor divides all possible combinations of energy deposited and the detector (or detectors) triggered, into 256 bins called event counters. An example of a counter would be “all events triggering only the A-F detector and depositing between 27 keV and 31 keV”. We will describe below the process by which an incident particle striking a detector results in the incrementing of one of these counters.

SEP uses a signal processing chain typical of particle detectors as shown schematically in Fig. 5. When a charged particle passes through or stops in one of the silicon detectors, it results in the creation of a quantity of electron-hole pairs proportional to the energy deposited. These pairs are accelerated by a  $\sim 40$  V bias potential across the detector and result in a voltage/current pulse, which is then amplified using Amptek 250F charge sensitive amplifiers. The signal is transmitted by coaxial cables to the Data Acquisition and Processing (DAP) board where it is shaped to a  $2.5 \mu\text{s}$  (zero to peak) unipolar Gaussian pulse. A threshold comparator is used to trigger a measurement if the pulse exceeds an adjustable threshold value. Peak detect circuitry is used to detect the peak in pulse height to sample the pulse magnitude with a 16 bit Analog-to-Digital Converter (ADC). A Field Programmable Gate Array (FPGA) controls the ADC triggering and readout and all subsequent event binning and telemetry production. Since the pulse height is proportional to the energy deposited, the ADC value is proportional to the energy deposited in the detector. All the detectors have depletion layers (or ‘dead’ layers) of a few hundred angstroms thickness at their surfaces, where no electron-hole pairs are present to record energy deposition. The open detectors have an additional  $\sim 900 \text{ \AA}$  of vapor-deposited aluminum that acts as an additional effective dead layer, hence the energy deposited in the ‘active’ volume of the detector is always lower than the total energy deposited. Energy lost to phonons and nuclear recoils is also not measured. These factors all contribute to pulse height defect and are accounted for in the instrument modelling. Note that more precise thicknesses of these dead layers were determined by laboratory calibrations and simulations (see Sect. 3.2). Each signal chain also includes a gated baseline restoration circuit that insures the baseline stays at zero voltage even at high count rates. The FPGA is programmed to periodically measure the baseline

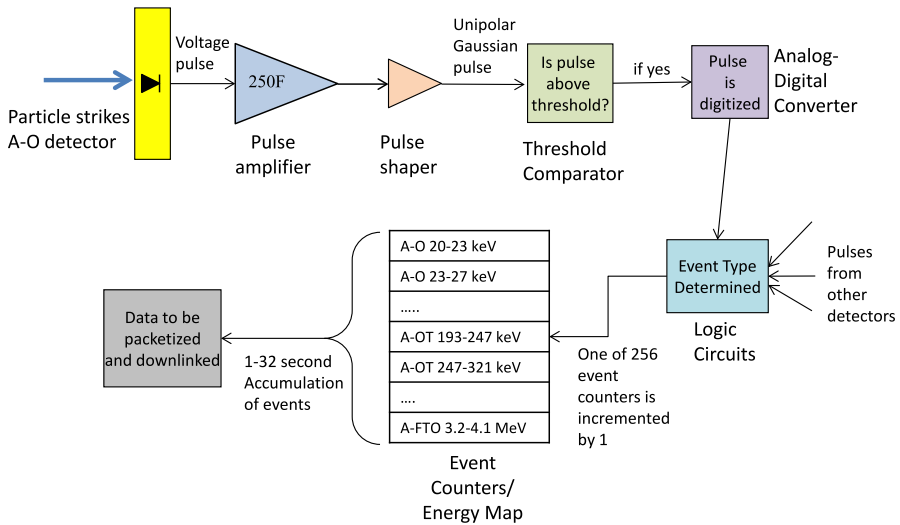


**Fig. 5** Schematic description of the SEP signal processing for the example of the A-O detector

signal in the absence of particle events and generates a 10 bin histogram for each channel. The baseline (aka pedestal) and noise level are determined from these histograms which are returned in the telemetry. The baseline level of every channel was tuned with trim resistors during assembly to produce an average bin value centered at zero.

Each channel has a test pulser with adjustable amplitude for testing in the absence of ionizing radiation. The test pulser can be used to verify the gain and baseline of each channel has not changed. It can not be used to detect changes in overall calibration since it does not respond to changes in pulse height defect in the detectors.

If an incident particle deposits more than  $\sim 11$  keV (the electronic noise threshold) in a detector, the voltage pulse is large enough to trigger an 'event' and the amount of energy deposited is digitized with a resolution of 1.36–1.54 keV (small differences exist across the 12 channels; see Table 3). Logic circuits characterize particle events by the combination of detectors which are simultaneously triggered (i.e. into which sufficient energy is deposited so that the pulse is detected). For example, an 'F' event is one in which the incident particle deposits all its energy in, and hence only triggers, the F detector. An 'FT' event is one in which both F and T detectors are simultaneously triggered, i.e. the particle passes through (and deposits energy in) the F detector, then deposits more energy and stops in the T detector.

Each event type (O, T, FTO, etc.) can be triggered by either an electron or an ion entering from one or both ends of each telescope. Figure 6 shows, with a table (left) and associated diagram (right), the approximate energy ranges and paths of electrons and ions that trigger F, FT, FTO, OT, and O events. FO events are considered to be two simultaneous separate F and O events. The energy ranges shown are taken directly from normal-incidence GEANT4 simulations. Figure 7 shows (from these simulations) the probability that a normally-incident electron or ion will be detected as a given event type. It shows that certain combinations of the event type and energy are unambiguous while others are ambiguous, i.e. an O event of 40 keV or 4 MeV must be an ion, but an O event of 500 keV could be electron or an ion. Thus the combination of the event type and energy are used as an anti-coincidence system to enable background subtraction. It also shows that FTO events cannot have a direction ascribed to them since the particle could have come through either aperture.

Incident energy ranges for counted events

	Electrons		Ions	
	Foil side keV	Open side keV	Foil side keV	Open side keV
No count	<20	<350	<250	<25
F	20-700		250-6000	
FT	350-1300		6000-11,000	
FTO	>600		>11,000	
OT		350-1300		6000-11,000
O		350-700		25-6000

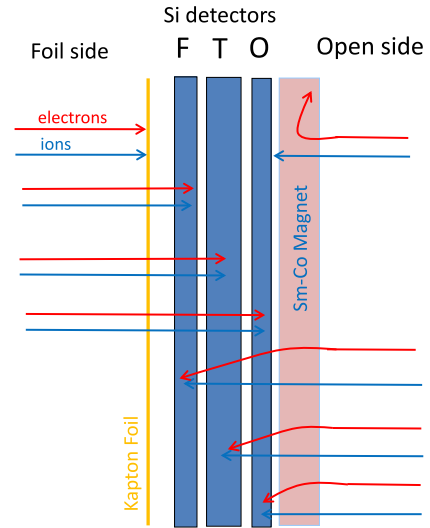


**Fig. 6** The particles and energies that result in different event types. The table on the left shows the approximate ranges of energies of electrons or ions coming from the foil or open side that will result in the different types of events (F, FT, FTO, OT, and O) recorded by the SEP sensor. The schematic diagram on the top right is aligned with each row of the table showing the paths of electrons (red) and ions (blue) from the foil or open side which results in these types of recorded events

The energy and type of each event determines which event counter will be incremented following the event. Each SEP sensor (i.e. SEP 1 and SEP 2) has 256 16-bit event counters which are shared by two telescopes (typically 128 bins per telescope). The event type and energy boundaries of each counter (e.g. all F events in the range 20–23 keV) are known as the ‘energy map’. Energy bins are spaced approximately logarithmically to provide a roughly constant dE/E. The better resolution at the low end of the SEP energy range allows better characterization of energy deposition to the Martian thermosphere. Figure 8 shows an example of an energy map, named “Flight3”. This map was used from Mars orbit insertion (September 21, 2014) until this paper went to press.

The 128 counters are read out via serial interface to the Particles in Fields Digital Processing Unit (PFDPU) every 1 second, where they are summed over the data acquisition interval of 2, 8 or 32 seconds before being packetized and sent to the ground in science data packets (APID 0 × 70 or 0 × 71). These arrays of event counters form the SEP Level 1 data. Level 2 data (i.e. fluxes of electrons and ions) require on-the-ground processing of these arrays of event counters, as described in Sect. 4.

### 3 SEP Calibration

On the ground, the aforementioned arrays of event counters must be processed into calibrated ion and electron spectra. This processing requires an accurate instrument calibration, i.e. measuring the detector response to particles of different types with a well-known energy. All calibration activities were performed in a custom vacuum chamber at the U.C. Berkeley Space Sciences Lab, made with attachments attached to both an electron and ion gun. Calibration of the SEP instrument requires two distinct steps, which will be described below.

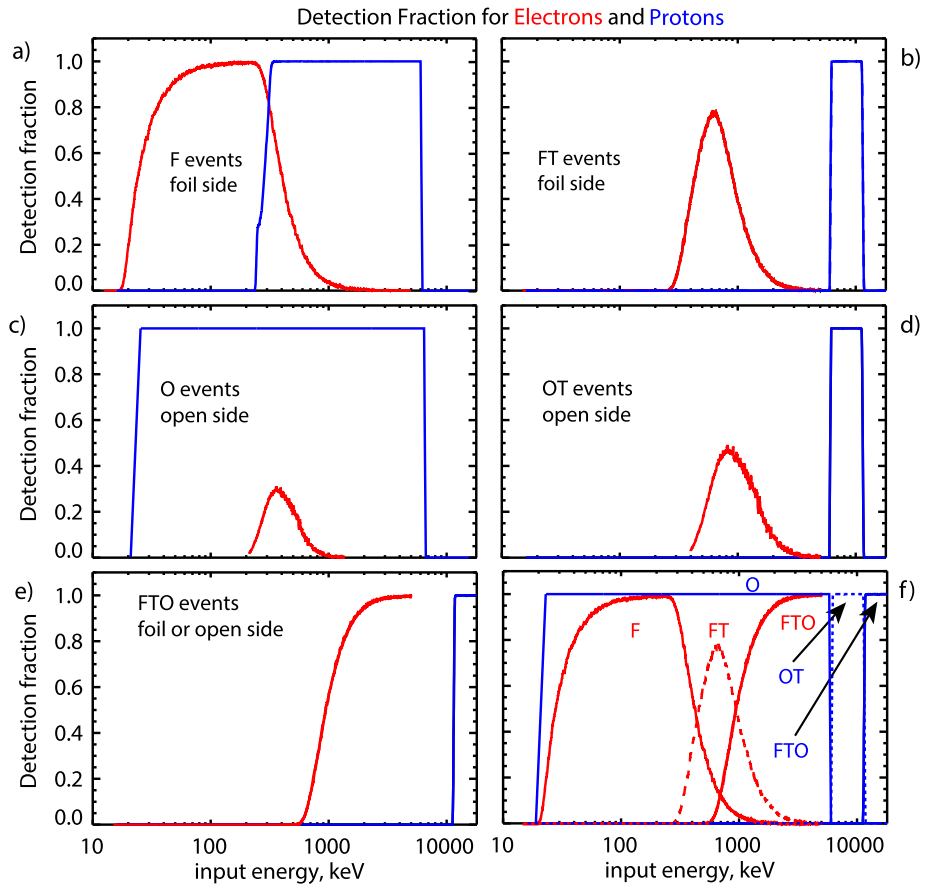


**Fig. 7** the probability that a normal-incidence electron or ion will be detected as a given type of event. Electron curves are shown *in red* and ion curves are shown *in blue*. Panels (a) and (b) in the *top row* show the fraction of electrons or ions from the foil side (see Figs. 4 and 6 schematic) that are detected a F or FT events respectively, as a function of energy. Panels (c) and (d) in the *second row* show the fraction of electrons or ions from the open side that are detected as O or OT events respectively, as a function of energy. Panel (e) shows the fraction of electrons or ions that are detected as FTO events; curves are nearly identical for foil or open side and so are not shown separately. Panel (f) shows *in red* probability curves for electrons coming from the foil side to be detected as F, FT or FTO events and *in blue* probability curves for protons coming from the open side to be detected as O, OT or FTO events

### 3.1 Absolute Energy Calibration

The first step is the absolute energy calibration, i.e. determining the relationship between the energy deposited and the digitized height of the amplified, shaped pulse output by the ADC. This is achieved by measuring the response to x-ray lines whose energies are very well-known, in this case the 59.54 keV line of radioactive Americium-241. Photons deposit energy in material primarily through three mechanisms: photoelectric effect, Compton scattering and pair production. Unlike charged particles, photons do not lose energy as they transit the dead layer. The cross section of low energy photons is dominated by the photoelectric effect and this interaction produces a narrow energy response at the photon energy, making them ideal for absolute energy calibration. Table 3 shows the number of ADC units

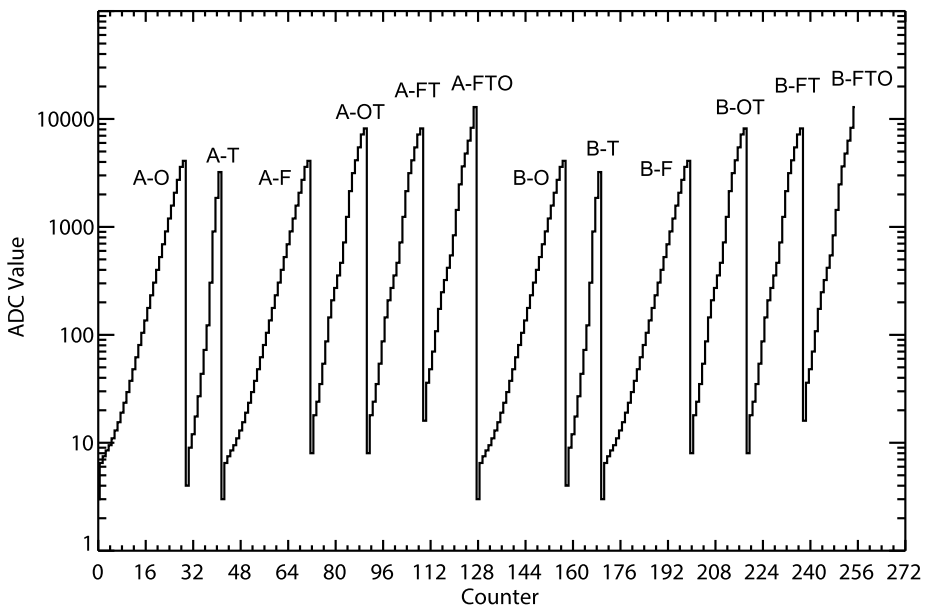


**Fig. 8** “Flight 3” instrument map showing the range of ADC values and event types for each of the 256 counters for each SEP sensor. The conversion from ADC value to particle energy is shown in Table 3. This map was used from Mars orbit insertion (September 21, 2014) until this article went to press

**Table 3** Number of ADC units per keV for each detector in each of the 2 SEP sensors

Detector	A-F	A-T	A-O	B-F	B-T	B-O
SEP 1	$0.690 \pm 0.025$	$0.646 \pm 0.032$	$0.735 \pm 0.024$	$0.711 \pm 0.024$	$0.677 \pm 0.032$	$0.705 \pm 0.022$
SEP 2	$0.738 \pm 0.026$	$0.741 \pm 0.034$	$0.676 \pm 0.023$	$0.705 \pm 0.023$	$0.739 \pm 0.034$	$0.726 \pm 0.024$

per keV and their uncertainties for each of the 12 SEP detectors. ADC units per keV are given instead of their inverse (often thought of as ‘gain’) because their uncertainties are symmetric. The baseline values (not shown) are all within 0.1 bins.

### 3.2 Ion Energy and Detector Dead Layer Calibration

The second calibration step is to determine the sensor response to charged particles, which can deposit energy in more than one detector and in other parts of the instrument. Since it was not possible to expose the SEP sensor to electrons and ions of all relevant energies (up to 1 MeV for electrons and ~ 13 MeV for protons), it is necessary to compare the charged particle response over a limited energy range with GEANT4 modelling (Agostinelli et al. 2003; Allison et al. 2006) of the detector response to the same range and find the model that provides the best fit to the instrument data.

Ground calibration for protons was performed with an ion gun at fixed proton energies of 25, 30, 35 and 40 keV (other ion species were filtered out using a Wien filter). Figure 9 shows an example for the detector A-O on the SEP 2 sensor of counts as a function of ADC value from the calibration test using the ion gun at 35 keV. The purpose of this was to characterize

**Fig. 9** SEP ion calibration example. Counts per second are plotted as a function of ADC value for an ion gun energy of 35 keV for detector SEP 2-A-O. The modeled values (*red*) are plotted against the measured values (*black*). The minor peak on the left is an artifact of the ion gun which produced a low energy population of protons. The low energy peak was not used in the fit

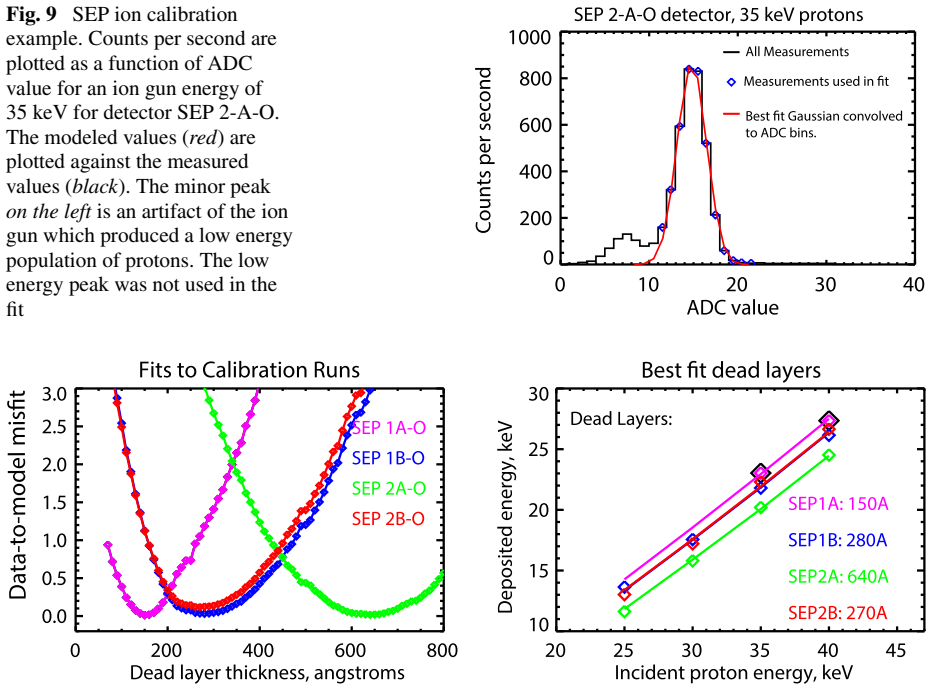


**Fig. 10** The *left panel* shows the data-to-model misfit as a function of dead layer thickness for the O detectors of each of the SEP detector stacks: 1A-pink, 1B-blue, 2A-green, 2B-red. The *right panel* shows, as unjoined diamonds, the measured deposited versus incident proton energy. The *solid lines* are the model results for the silicon dead layer thickness that best fits the measurements, using the same color legend

the thickness of the effectively dead layer of Si and Al on each of the four O detectors. The Al dead layer was held fixed at the manufacturer-specified 900 Å and the Si dead layer (modeled as a step-function transition from active to dead) was varied from 50 to 800 Å in the GEANT4 proton simulations. All contributions to pulse height defect (phonons, nuclear recoils, energy lost in the dead layer) are modeled by GEANT4 and therefore included in the calibration. The misfit between the energy measured by the instrument and the energy deposited in the detector in the simulation was calculated. Figure 10 shows the shape of the misfit curves as a function of modeled dead layer thickness (left) and the comparison of the best-fit modeled proton response curves to the measured proton response (right). The best-fit effective dead layer thicknesses for SEP1A, SEP1B, SEP2A and SEP2B are 150, 280, 640 and 270 Å respectively. In a real detector the transition from dead to active silicon is not a step function (i.e. it occurs over a finite distance) but our modeling of this sharp ‘effective’ dead layer is sufficient to characterize the response of the ‘open’ detectors.

### 3.3 SEP Electron Calibration

The third calibration step is to determine the sensor response to electrons. An electron gun was aimed at the sensor in vacuum, while the electron energy was slowly increased from 10 keV up to 40 keV (Fig. 11, top panel). The raw calibration results are shown in Fig. 11 (middle panel). The first detectable counts (i.e. energy depositions that produce a signal above the electronic noise threshold of ~ 11 keV) begin around the incident electron energies of ~ 14 keV, as shown in the middle panel). The peak in the spectrum was determined

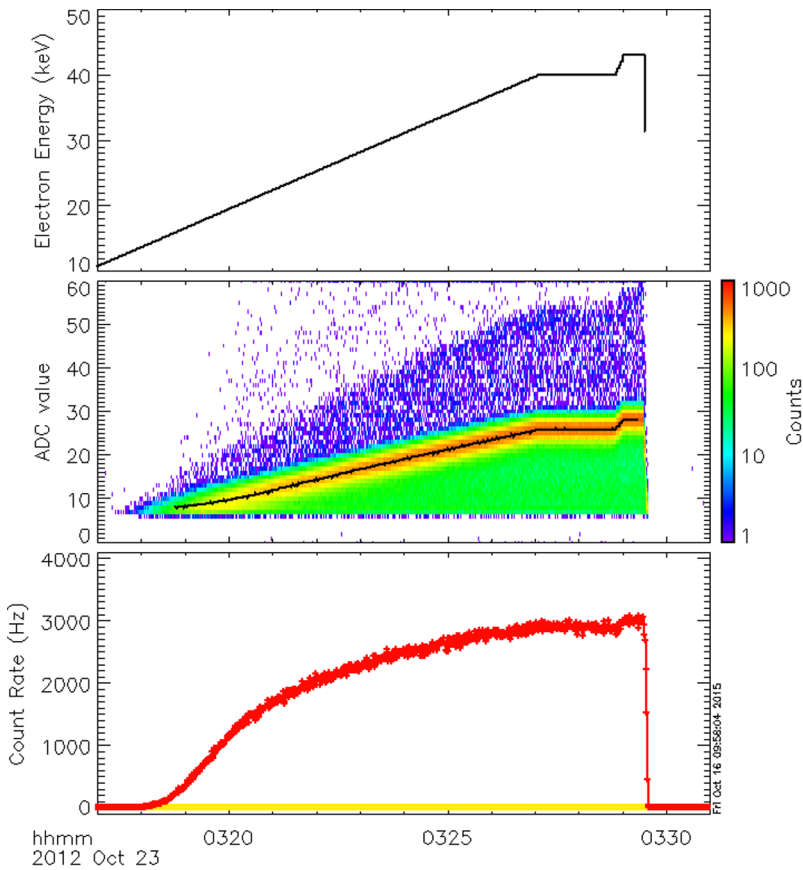
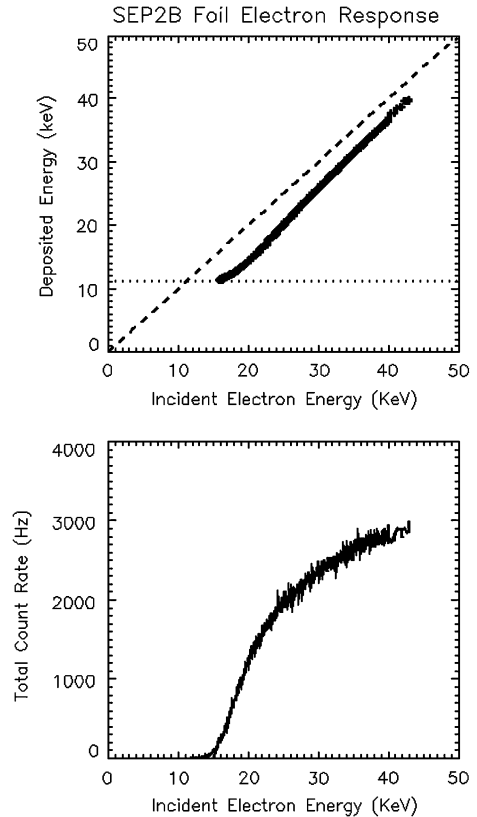


**Fig. 11** Raw data showing the SEP2B instrument response to incident electrons. The *top panel* shows the incident electron energy. The *middle panel* shows the count rate in each ADC bin. The *black line* shows the ADC bin where the maximum in counts occurs. The *bottom panel* shows the total count rate (proportional to total efficiency)

for each incident energy. Sensitivity of the sensors to electrons is robust for incident energies above 20 keV. The middle panel shows there is a significant response in ADC bins at all energies below the peak (overlaid with a black line). This is a typical response caused by electrons that enter the active region of the detector and then backscatter out of the detector before they can deposit their full energy. This effect is observed in GEANT4 simulations. There is an additional, though much weaker, response in ADC bins that correspond to deposited energies at 2 or 3 times the incident electron energy (see blue/violet shaded region of Fig. 11, middle panel). This is the result of the pulse pileup when two or more electrons hit the detector at the same time. This effect is accentuated by the generation of electrons in the gun. These electrons are generated by UV photons impinging on a photocathode that is held at a large negative voltage. Since the photocathode is powered by an AC supply there is an increased probability of the production of simultaneous photons and subsequent electrons. The bottom panel shows the total count rate summed over all bins.

Figure 12 (top panel) shows the peak in the response function (Fig. 11, middle panel) plotted against the corresponding incident electron energy (Fig. 11, top panel), compared

**Fig. 12** (*Top panel*) measured electron energy vs. incident electron energy derived from the data shown in Fig. 11 and using the gain from Table 3. The *horizontal dotted line* marks the electronic noise threshold of  $\sim 11$  keV. (*Bottom panel*) total count rate vs. incident electron energy



with a perfect ‘lossless’ detector (dashed line). The difference between the dashed line and the solid line represents the energy lost in the Kapton foil (and dead layer), which is typically less than 5 keV). The response curve should not be trusted near the low-energy end where the measured energy is just above the electronic noise threshold value ( $\sim 11$  keV, marked by the horizontal dashed line). The bottom panel of Fig. 12 shows the count rate as a function of incident electron energy, representing the relative detection efficiency as a function of electron energy. Note that the absolute efficiency can only be determined from GEANT4 modeling.

## 4 SEP Data and Operation

### 4.1 Deconvolution of Electron and Ion Spectra

Knowledge of the dead layer thicknesses of each of the O detectors, along with a detailed knowledge of the mechanical structure and material properties of the sensor, allows for accurate modeling of the detector response to a wide range of electron and ion energies via GEANT4 simulations. It is particularly important to separate the contamination effects of electrons and ions on the same event type (e.g. a 250 keV proton entering the foil side collimator loses between 170 and 250 keV in the foil and deposits 0 to 80 keV in the F detector,

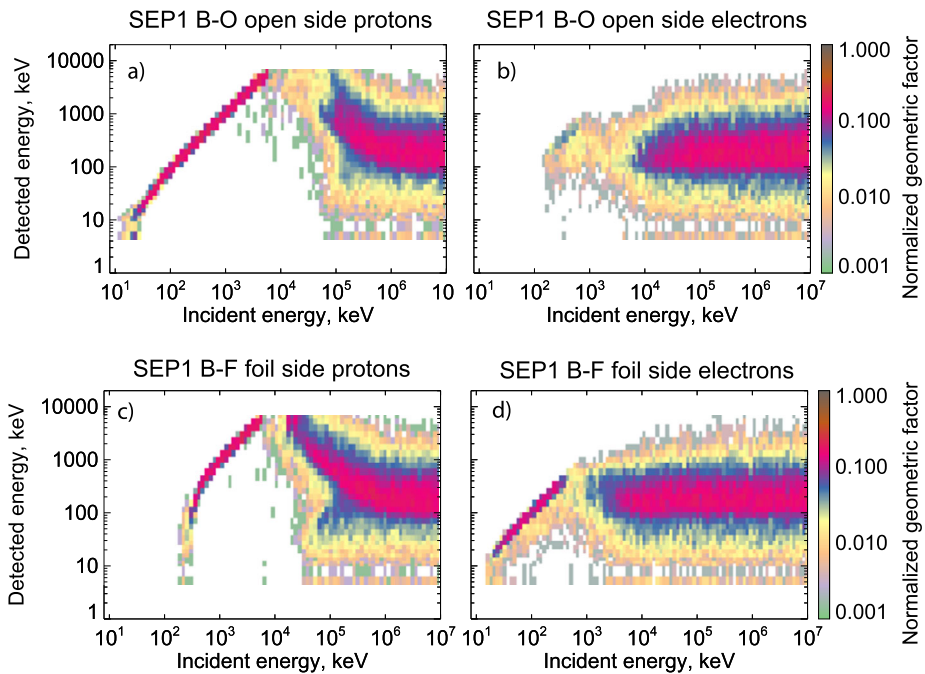


**Fig. 13** Four example response matrices derived from GEANT4 simulations. Panels (a) and (b) show the normalized geometric factor for protons and electrons respectively, coming from the front side of the SEP 1 sensor and causing ‘O’ energy deposition events in the ‘B’ telescope while the attenuator is open. Panels (c) and (d) show the normalized geometric factor for protons and electrons respectively, coming from the rear side of the SEP 1 sensor and causing ‘F’ energy deposition events in the ‘B’ telescope. This demonstrates that electrons never significantly contaminate the ion measurement in the O detector, but that ions can and do significantly contaminate the electron measurement in the F detector

mimicking an electron of that energy) and to model background counts caused by galactic cosmic rays penetrating the instrument housing.

Even though the electronic noise threshold is  $\sim 11$  keV, the energy losses mentioned above mean the effective low-energy threshold is  $\sim 20$  keV for electrons and  $\sim 25$  keV for ions and varies slightly by detector (see Fig. 6a, left).

For each of the instrument maps (e.g., Fig. 8) and for each SEP sensor, a set of response matrices were derived from GEANT4 simulations. Matrices were derived for both telescopes within each sensor (A and B), 6 event types (F, T, O, FT, OT, FTO), 4 particle types (electrons, protons, alphas and photons), 2 attenuator state (open and closed) and 2 particle directions (forward and reverse look directions), totaling 192 response matrices. These matrices constitute a forward model for converting electron and ion energy spectra in 4 look directions into count rates in 256 counters in each SEP sensor. Figure 13 shows 4 of such response matrices for the “Flight3” instrument map shown in Fig. 8.

The GEANT4 modeling provides the best estimate of original particle energy and detection efficiency for each accumulation bin. Using these values, the count rates in each of the ‘O’ channels provide a zero order estimate of the ion flux in four look directions (all ions are assumed to be protons). Likewise the ‘F’ channel count rates provides a zero order estimate of electron fluxes. Typically the ‘O’ channels do not have a significant level of contamination from electrons because the broom magnets are very effective at sweeping

away lower energy electrons ( $< 250$  keV) and the more energetic electrons ( $> 350$  keV) will typically pass through the first 'O' detector and are not counted as 'O' events due to anticoincidence (this is shown in Fig. 13b where electrons have a tiny geometric factor for B-O events below  $\sim 10$  MeV). In addition, the ions fluxes are typically higher for a given energy than the electron fluxes. However, the zero order electron fluxes are often heavily contaminated by ions—especially at energies greater than  $\sim 250$  keV because these ions, up to 6 MeV, cause 'F' events (see Figs. 6, 7 and 13c). The zero order ion flux estimate is convolved with the appropriate response matrix to estimate the level of contamination in the foil detector with the same FOV. These contamination counts are subtracted and the electron fluxes are then recomputed. A similar process is used to estimate contamination of ions from the electrons. The first order corrections correspond to the Level 2 data archived at the PDS as of the date of publication of this article. Uncertainties in the fluxes are based on standard Poisson statistics. Figure 14 shows an example of data from the SEP 1 sensor. The top panel shows both the raw count rate in each of the 256 counters (see Fig. 5). In the third to sixth panels, the data have been converted to differential energy flux spectra (mostly proton and up to 20 % alpha particle) and electron differential energy flux spectra resulting from the aforementioned process are shown.

A more refined method of computing the ion and electron fluxes is to use the forward model to fit for the electrons and ion fluxes that simultaneously best fit the measured count rates in each of the 256 counters. In other words, this fitting is an attempt to subtract ion contributions from the electron spectra and vice versa. This method has not yet been implemented for the Level 2 data product.

Upon arrival at Mars, it was learned that Pick-Up Oxygen (PUO) ions sometimes represents a very significant contribution to the ion fluxes especially in the Forward looking detectors at (measured) energies less than 100 keV. These PUO can only be observed during periods of high solar wind velocity ( $> 500$  km/s) and with favorable magnetic field orientation. The PUO flux can have a very narrow angular extent and the observed flux can vary by orders of magnitude in as little as 8 seconds. The disambiguation between Oxygen and Protons has not been resolved in the L2 data distribution at this time.

Other forms of contamination are present. X-rays from large flares can produce counts in all non-coincident channels ('O', 'T' and 'F') these are particularly apparent in the 'T' channels since this channel is essentially devoid of contamination from electrons and ions. Penetrating particles, i.e. Galactic Cosmic Rays (GCRs) can produce events in all channels but are most likely to generate coincident ('OT', 'FT' and 'FTO') events. The GCRs produce a nearly constant FTO rate of 1.4 events/sec. Since GCRs are minimum ionizing events ( $\sim 120$  keV deposited per detector) the FTO events typically deposit  $\sim 500$  keV in the FTO channel (i.e. 4 times the minimum ionizing energy from two thin F and O detectors and the double-thickness T detector).

Another source of contamination is the attenuator actuation. Every actuation produces  $\sim 40$  counts in a single accumulation cycle. Whenever the PFDPU actuates (or polls the status of) the attenuators on STATIC or SWIA there can be contamination counts. These are typically rare and can only be noticed during quiet times. When the spacecraft is oriented such that the Sun is in the FOV of one of the open detectors the increased leakage current results in an increase in detector noise and also a subsequent increase in the count rate of the lowest energy channel.

## 4.2 SEP Commanding

The SEP instrument is commanded through the PFDPU in two primary ways. First, the instrument FPGA can be commanded directly using CDI (Command and Data Interface)

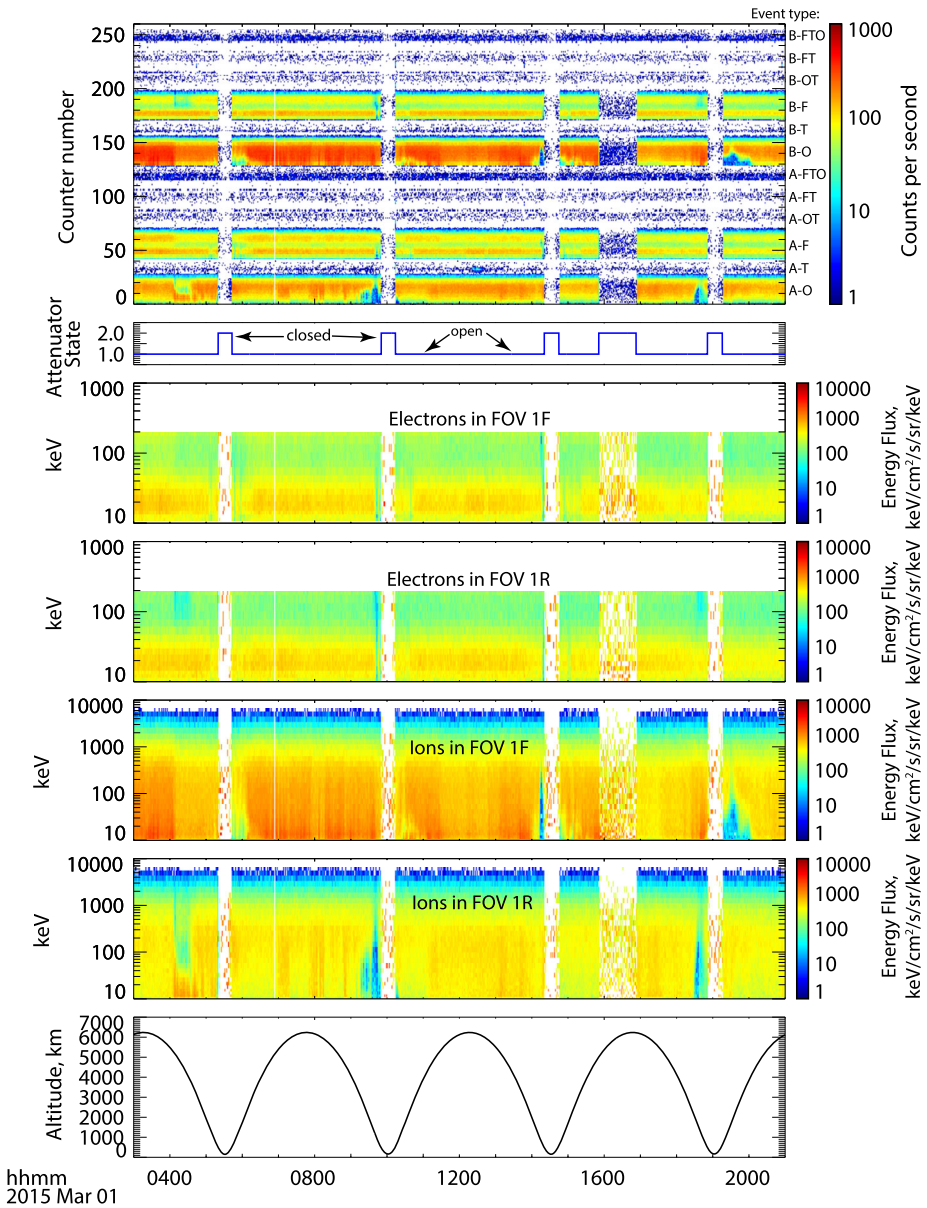


**Fig. 14** Data example from SEP Sensor 1 over 18 hours on March 1, 2015. The *top panel* shows the number of counts per second in each of the 256 onboard counters (the same counters associated with energy & ADC ranges in Fig. 8). The *second panel* shows the state of the attenuator (2 = closed, 1 = open); when closed the flux is reduced by a factor of  $\sim 100$ . The *third to sixth panels* show the reconstructed fluxes of electrons and ions (mostly protons) in the 1F and 1R look directions (as shown in Fig. 3). The *bottom panel* shows the MAVEN spacecraft altitude for context

protocol or flight software function calls to perform several kinds of operations: memory operations (load new energy maps) and memory tests, change the bias voltage on the detectors, change their preamplifier voltage thresholds (i.e. above which a voltage pulse qualifies as a count), disable/enable housekeeping and science messages, open and close the attenuators and control the test pulser (used for diagnosing issues or anomalies). Second, a sequence of CDI or flight software commands known as an RTS (or Real Time Sequence) can be preloaded into the EEPROM (memory) in the PFDPU and executed on board. The PFDPU uses RTS calls to power off and on the SEP instrument and to change telemetry rates, as mentioned in the section below.

### 4.3 Attenuator Control

The SEP attenuator extends the dynamic range of sensitivity of the sensors by a factor of  $\sim 100$ . The dead time corrections become significant when the count rate of a single detector exceeds 30 kHz. Thus, whenever the count rate of a single detector exceeds a programmable threshold (typically 20 kHz) all four attenuator paddles for that sensor will swing into place. This action is performed by the PFDPU.

In addition to providing increased dynamic range, the SEP attenuators play a safety role in protecting the detectors from direct sunlight, which can permanently damage the detectors after just a few minutes of exposure. Therefore, the MAVEN spacecraft has separate direct control over each of the attenuator mechanisms (on sensors 1 and 2): a spacecraft zone alert closes them at times when the Sun is in the field of view of that sensor. An example of just such a closure is shown in Fig. 14, just after 1600 hrs.

During the cruise phase, a serious concern arose regarding SEP detector damage by atomic oxygen in Mars' upper atmosphere. Therefore, the SEP attenuators are automatically closed below 300 km in all cases and below 500 km when the FOV are within  $30^\circ$  of the spacecraft velocity vector. This is seen in Fig. 14 at approximately times 0530, 1000, 1430 and 1900 UT.

### 4.4 Modes & Telemetry Rates

SEP is a purposely 'dumb' instrument in the sense that it only has one hardware mode; it collects data continuously at a 1 second cadence in the same manner. The PFDPU sums this data into 1-, 2-, 8- or 32-second accumulations to be downlinked to Earth, depending on spacecraft altitude and Earth-Mars downlink rates. As an example, from November 2014 until February 2015, the SEP time cadence was at its highest: 2 seconds below 300 km altitude and 8 seconds everywhere else in the orbit.

## 5 Conclusions

The SEP instrument exceeds all its Level 1 mission requirements and makes an important measurement for the MAVEN mission, providing a characterization of high energy solar and interplanetary charged particles in the Mars environment. This allows us to quantify the energy input to the Martian atmosphere from these particles and therefore to understand their effects on the structure and dynamics of the atmosphere, as well as how this impacts atmospheric escape from Mars.

In addition to the important role it plays in the MAVEN science, the SEP instrument can operate as a heliospheric space weather monitoring station for high-energy particles

as they propagate out from the Sun and from interplanetary shocks caused by fast coronal mass ejections. The comparison of particle fluxes measured by SEP with those measured at L1 and along the orbit at 1 AU by the Solar TERrestrial RELations Observatory (STEREO) (Kaiser 2005) A and B spacecraft will undoubtedly assist in improving our understanding of the propagation and evolution of heliospheric disturbances. Moreover, with MSL RAD at the surface, we can determine to first order whether there are ground-level effects due to SEPs during active solar event periods. At the same time, the MAVEN SEP observations can provide the space weather context for the solar-activity dose rates measured by RAD at the surface.

## References

- S. Agostinelli, J. Allison, K. Amako, J. Apostolakis, H. Araujo et al., GEANT4—a simulation toolkit. *Nucl. Instrum. Methods Phys. Res.* **506**, 250–303 (2003)
- J. Allison, K. Amako, J. Apostolakis, H. Araujo, P. Arce Dubois et al., Geant4 developments and applications. *IEEE Trans. Nucl. Sci.* **53**, 270–278 (2006)
- L. Andersson, R.E. Ergun, G. Delory, The Langmuir probe and waves experiment for MAVEN. *Space Sci. Rev.* (2015). doi:[10.1007/s11214-015-0194-3](https://doi.org/10.1007/s11214-015-0194-3)
- V. Angelopoulos, D. Sibeck, C.W. Carlson et al., First results from the THEMIS mission. *Space Sci. Rev.* (2008). doi:[10.1007/s11214-008-9378-4](https://doi.org/10.1007/s11214-008-9378-4)
- S. Barabash et al., The analyzer of space plasmas and energetic atoms (ASPERA-3) for the Mars express mission. *Space Sci. Rev.* **126**, 113–164 (2006). doi:[10.1007/s11214-006-9124-8](https://doi.org/10.1007/s11214-006-9124-8)
- J.-L. Bertaux, F. Leblanc, O. Witasse, E. Quemerais, J. Liliensten, S.A. Stern, B. Sandel, O. Korablev, Discovery of an aurora on Mars. *Nature* **435**, 790–794 (2005). doi:[10.1038/nature03603](https://doi.org/10.1038/nature03603)
- M.W. Chevalier, W.B. Peter, U.S. Inan, T.F. Bell, M. Spasojevic, Remote sensing of ionospheric disturbances associated with energetic particle precipitation using the South Pole VLF beacon. *J. Geophys. Res.* **112**, A11306 (2007). doi:[10.1029/2007JA012425](https://doi.org/10.1029/2007JA012425)
- J.E.P. Connerney, J. Espley, P. Lawton, S. Murphy, J. Odom, R. Oliverson, D. Sheppard, The Maven magnetic field investigation. *Space Sci. Rev.* (2015). doi:[10.1007/s11214-015-0169-4](https://doi.org/10.1007/s11214-015-0169-4)
- A.V. Dmitriev, H.-C. Yeh, Geomagnetic signatures of sudden ionospheric disturbances during extreme solar radiation events. *J. Atmos. Sol.-Terr. Phys.* **70**, 1971–1984 (2008). doi:[10.1016/j.jastp.2008.05.008](https://doi.org/10.1016/j.jastp.2008.05.008)
- F. Eparvier, P.C. Chamberlin, T.N. Woods, E.M.B. Thiemann, The solar extreme ultraviolet monitor for MAVEN. *Space Sci. Rev.* (2015). doi:[10.1007/s11214-015-0195-2](https://doi.org/10.1007/s11214-015-0195-2)
- J.R. Espley, W.M. Farrell, D.A. Brain, D.D. Morgan, B. Cantor, J.J. Plaut, M.H. Acuña, G. Picardi, Absorption of MARSIS radar signals: Solar energetic particles and the daytime ionosphere. *Geophys. Res. Lett.* **34**, L09101 (2007). doi:[10.1029/2006GL028829](https://doi.org/10.1029/2006GL028829)
- Y. Futaana et al., Mars express and Venus express multi-point observations of geoeffective solar flare events in December 2006. *Planet. Space Sci.* **56**(6), 873–880 (2008)
- J.S. Halekas, E.R. Taylor, G. Dalton, G. Johnson, D.W. Curtis, J.P. McFadden, D.L. Mitchell, R.P. Lin, B.M. Jakosky, The solar wind ion analyzer for MAVEN. *Space Sci. Rev.* (2013). doi:[10.1007/s11214-013-0029-z](https://doi.org/10.1007/s11214-013-0029-z)
- D.M. Hassler et al., The radiation assessment detector (RAD) investigation. *Space Sci. Rev.* **170**, 503–558 (2012). doi:[10.1007/s11214-012-9913-1](https://doi.org/10.1007/s11214-012-9913-1)
- D.M. Hassler et al., Mars' surface radiation environment measured with the Mars science laboratory's curiosity rover. *Science* **343** (2014). doi:[10.1126/science.1244797](https://doi.org/10.1126/science.1244797)
- B.M. Jakosky, R.P. Lin, J.M. Grebowsky, J.G. Luhmann, D.F. Mitchell, G. Beutelschies et al., The Mars atmosphere and volatile evolution (MAVEN) mission. *Space Sci. Rev.* (2014). doi:[10.1007/s11214-015-0139-x](https://doi.org/10.1007/s11214-015-0139-x)
- M. Kaiser, The STEREO mission: An overview. *Adv. Space Res.* **36**, 1483 (2005)
- F. Leblanc, O. Witasse, J. Wittingham, D. Brain, J. Liliensten, P.-L. Blelly, R.A. Frahm, J.S. Halekas, J.L. Bertaux, Origins of the Martian aurora observed by spectroscopy for investigation of characteristics of the atmosphere of Mars (SPICAM) on board Mars express. *J. Geophys. Res.* **111**, A09313 (2006). doi:[10.1029/2006JA011763](https://doi.org/10.1029/2006JA011763)
- R.J. Lillis, D.A. Brain, G.T. Delory, D.L. Mitchell, J.G. Luhmann, R.P. Lin, Evidence for superthermal secondary electrons produced by SEP ionization in the Martian atmosphere. *J. Geophys. Res.* **117**, E03004 (2012). doi:[10.1029/2011JE003932](https://doi.org/10.1029/2011JE003932)

- R.J. Lillis, D.A. Brain, S.W. Bougher, F. Leblanc, J.G. Luhmann, B.M. Jakosky, R. Modolo, J. Fox, J. Deighan, X. Fang, Y.C. Wang, Y. Lee, C. Dong, Y. Ma, T. Cravens, L. Andersson, S.M. Curry, N. Schneider, M. Combi, I. Stewart, J. Clarke, J. Grebowsky, D.L. Mitchell, R. Yelle, A.F. Nagy, D. Baker, R.P. Lin, Characterizing atmospheric escape from Mars today and through time, with MAVEN. *Space Sci. Rev.* (2015). doi:[10.1007/s11214-015-0165-8](https://doi.org/10.1007/s11214-015-0165-8)
- R.P. Lin et al., A 3-dimensional plasma and energetic particle investigation for the wind spacecraft. *Space Sci. Rev.* **71**(1–4), 125–153 (1995)
- R.P. Lin, D.W. Curtis, D.E. Larson, J.G. Luhmann, S.E. McBride, M.R. Maier, T. Moreau, C.S. Tindall, P. Turin, L. Wang, The STEREO IMPACT suprathermal electron (STE) instrument. *Space Sci. Rev.* (2008). doi:[10.1007/s11214-008-9330-7](https://doi.org/10.1007/s11214-008-9330-7)
- P.R. Mahaffy, M. Benna, T. King et al., The neutral gas and ion mass spectrometer on the Mars atmosphere and volatile evolution mission. *Space Sci. Rev.* (2014). doi:[10.1007/s11214-014-0091-1](https://doi.org/10.1007/s11214-014-0091-1)
- W.E. McClintock, N.M. Schneider, G.M. Holsclaw, J.T. Clarke, A.C. Hoskins, I. Stewart, F. Montmessin, R.V. Yelle, J. Deighan, The imaging ultraviolet spectrograph (IUVS) for the MAVEN mission. *Space Sci. Rev.* (2014). doi:[10.1007/s11214-014-0098-7](https://doi.org/10.1007/s11214-014-0098-7)
- J. McFadden, O. Kortmann, G.J. Dalton, R. Abiad, D. Curtis, R. Sterling, K. Hatch, P. Berg, C. Tiu, M. Marckwordt, R. Lin, B. Jakosky, The MAVEN suprathermal and thermal ion composition (STATIC) instrument. *Space Sci. Rev.* (2015)
- S.V. McKenna-Lawlor, V. Afonin, K.I. Gringauz, K. Kecskemeti, E. Keppler, f.F. Kirsch, f.A. Richter, P. Ruzsnyak, K. Schwingenschuh, D. O’Sullivan, A.J. Somogyi, L. Szabo, A. Thompson, A. Varga, Ye. Yeroshenkoll, M. Witte, Energetic particle studies at Mars by SLED on Phobos-2. *Adv. Space Res.* **12**(9), 231–241 (1992)
- D.L. Mitchell, R.P. Lin, C. Mazelle, H. Rème, P.A. Cloutier, J.E.P. Connerney, M.H. Acuna, N.F. Ness, Probing Mars’ crustal magnetic field and ionosphere with the MGS electron reflectometer. *J. Geophys. Res.* **106**(E10), 23419–23427 (2001). doi:[10.1029/2000JE001435](https://doi.org/10.1029/2000JE001435)
- D.D. Morgan, D.A. Gurnett, D.L. Kirchner, R.L. Huff, D.A. Brain, W.V. Boynton, M.H. Acuña, J.J. Plaut, G. Picardi, Solar control of radar wave absorption by the Martian ionosphere. *Geophys. Res. Lett.* **33**, L13202 (2006). doi:[10.1029/2006GL026637](https://doi.org/10.1029/2006GL026637)
- R. Müller-Mellin, S. Böttcher, J. Falenski, E. Rode, L. Duvet, T. Sanderson, B. Butler, B. Johlander, H. Smit, The solar electron and proton telescope for the STEREO mission. *Space Sci. Rev.* **136**(1–4), 363–389 (2008). doi:[10.1007/s11214-007-9204-4](https://doi.org/10.1007/s11214-007-9204-4)
- J.B. Reagan, T.M. Watt, Simultaneous satellite and radar studies of the D region ionosphere during the intense solar particle events of August 1972. *J. Geophys. Res.* **81**(25), 4579–4596 (1976). doi:[10.1029/JA081i025p04579](https://doi.org/10.1029/JA081i025p04579)
- C. Zeitlin, T. Cleghorn, F. Cucinotta, P. Saganti, V. Andersen, K. Lee, L. Pinsky, W. Atwell, R. Turner, G. Badhwar, Overview of the Martian radiation environment experiment. *Adv. Space Res.* **33**(12), 2204–2210 (2004)